Spatial and Temporal Noise in Solar EUV Observations

V. Delouille · P. Chainais · J.-F. Hochedez

Abstract Solar telescopes will never be able to resolve the smallest events at their intrinsic physical scales. Pixel signals recorded by SOHO/(CDS, EIT, SUMER), STEREO/SECCHI/EUVI, TRACE, SDO/AIA, and even by the future *Solar Orbiter* EUI/HRI contain an inherent "spatial noise" since they represent an average of the solar signal present at subpixel scales. In this paper, we aim at investigating this spatial noise, and hopefully at extracting information from subpixel scales. Two paths are explored. We first combine a regularity analysis of a sequence of EIT images with an estimation of the relationship between mean and standard deviation, and we formulate a scenario for the evolution of the local signal-to-noise ratio (SNR) as the pixel size becomes smaller. Second, we use an elementary forward modeling to examine the relationship between nanoflare characteristics (such as area, duration, and intensity) and the global mean and standard deviation. We use theoretical distributions of nanoflare parameters as input to the forward model. A fine-grid image is generated as a random superposition of those pseudo-nanoflares. Coarser resolution images (simulating images acquired by a telescope) are obtained by rebinning and are used to compute the mean and standard deviation to be analyzed. Our results show that the local SNR decays more slowly in regions exhibiting irregularities than in smooth regions.

V. Delouille (✉) · J.-F. Hochedez
SIDC – Royal Observatory of Belgium, Brussels, Belgium
e-mail: v.delouille@oma.be

J.-F. Hochedez
e-mail: hochedez@oma.be

P. Chainais
Université Blaise Pascal Clermont II, Clermont-Ferrand, France
e-mail: pchainai@isima.fr

1. Introduction

Future missions such as *Solar Orbiter* (SO) aim at studying the Sun from closer than ever. It is expected that the High Resolution Imagers (HRI) onboard SO will have a pixel size of 0.5 arcsec and a cadence better than one second (Hochedez *et al.*, 2001). When the SO mission is at perihelion (*i.e.*, at a distance of 0.2 AU from the Sun), one pixel of HRI will represent approximately (80 km^2) on the Sun. Note that 80 km corresponds to a pixel size of 0.1 arcsec for an instrument located at 1 AU.

Under these conditions it is unclear whether there will be enough photons per pixel to illuminate the detector and whether the signal-to-noise ratio (SNR) will be sufficient. It is thus necessary to quantify the expected level of SNR, and more generally to provide tools for extracting information from subpixel scales. We propose two ways to get new insights into this issue.

First, the analysis of a high-cadence data set recorded by the EIT instrument (Delaboudinière *et al.*, 1995) on 4 October 1996 allows us to describe how the *local* SNR evolves as the scale of observation (or pixel size) becomes smaller. We show that the decrease in SNR as the resolution gets finer is not the same when the spatial fluctuations of the radiance are taken into account or when a uniform radiance is considered. Indeed, the photon emission process can be modeled by a Poisson distribution Po(L), where L represents the radiance. If the emission of the solar corona were uniform over the entire Sun, we would have an homogeneous Poisson process. Denoting by μ_a the mean intensity recorded and by σ_a the corresponding standard deviation (STD), we have that the SNR would simply linearly decrease as a function of the scale (a) of observation: $\mu_a/\sigma_a \sim a$. Fortunately, different parts of the corona have different levels of emission; that is, the photon flux that hits the detector at a particular location ($\mathbf{x}$) during an exposure time (T) follows an *inhomogeneous* Poisson distribution Po[$L(\mathbf{x}, T)$], where the radiance L is space and time dependent. Let us consider that $L(\mathbf{x}, T_0) = f(\mathbf{x})L_0$ for some given exposure time (T_0), with L_0 a constant and $f(\mathbf{x})$ a function describing the inhomogeneities in a solar coronal image. Our purpose is to study how the local variations of $f(\mathbf{x})$ influence the local SNR.

In the second part of the paper, we propose a basic forward modeling technique that takes as input different distributions of flare characteristics proposed in the literature (Crosby *et al.*, 1993; Isliker *et al.*, 2001; Krucker and Benz, 1998; Paczuski *et al.*, 2005; Vlahos *et al.*, 1995). We emulate the instrument response through rebinning. The forward model gives as output the average (μ_a) and standard deviation (σ_a), computed either over space or over time. We confirm that the relationship $\sigma_a = b_0\mu_a^{b_1}$ prevails, similarly to what is observed in real data, and we investigate how the coefficient b_1 is influenced by pseudo-nanoflare distribution parameter values.

This paper is organized as follows: Section 2 recalls the various sources of noise that impact the quality of EIT images and explains how to access subpixel information by using a high-cadence EIT data set. Section 3 introduces our forward modeling approach and presents the results of the corresponding simulation study. Finally, Section 4 places our work in perspective with other studies on noise in solar images and gives prospects for future research.

2. EIT Data Set Analysis

The aim of this section is to estimate subpixel variability within a high-cadence EIT sequence. We begin by recalling the main sources of error present in EIT images.

2.1. Sources of Noise in EIT Images

The incident EUV flux of interest on EIT is converted in digital numbers (DN) through a series of steps. At each step, some noise may be introduced. In brief, the beam of photons impinges the optical system where the optical point-spread-function (PSF) acts as a blurring operator. Simultaneously, a spectral selection is performed on the signal before it reaches the CCD detector. The latter has a heterogeneous response across its surface. Finally, the camera electronics convert photon counts into DN; this conversion adds the read-out noise.

2.1.1. Poisson Noise

The photon emission processes in the solar atmosphere are random and incoherent in nature. They are usually modeled by a Poisson process so that the number of incident photons between t and $t + T$ obeys a Poisson law $\text{Po}[L(\mathbf{x}, t, T)]$ of mean $L(\mathbf{x}, t, T)$, where the radiance L is space and time dependent. When L is sufficiently large ($L > 1000$), the Poisson distribution may be approximated by a Gaussian. Lower photon counts give higher variance with respect to the mean and hence smaller SNR. Let $N(\mathbf{x})$ denote the number of photons that hit the detector at location $\mathbf{x}$, time t_0, and during an exposure time T_0. $N(\mathbf{x})$ is modeled by a Poisson random variable distributed as $\text{Po}[L(\mathbf{x}, t_0, T_0)]$. The recorded signal $S(\mathbf{x})$ measured in DN at location $\mathbf{x}$ is equal to (Defise, 1999; Janesick *et al.*, 1985)

$$S(\mathbf{x}) = qN(\mathbf{x}), \quad q = \text{QE} \cdot \eta_i \cdot \frac{1}{G}, \tag{1}$$

where QE is the inner quantum efficiency (in number of detected photons per incident photon), η_i is the ideal quantum yield (in electrons per detected photon), and G is the electronic gain (in electrons per DN).

Since $N(\mathbf{x})$ can be viewed as a realization from a random variable, so is $S(\mathbf{x})$. Its mathematical expectation denoted by $E[S(\mathbf{x})]$ is equal to $\mu(\mathbf{x}) \equiv E[S(\mathbf{x})] = qL(\mathbf{x})$. The variance of $S(\mathbf{x})$ is given by

$$\sigma(\mathbf{x})^2 \equiv \text{Var}\big[S(\mathbf{x})\big] = q^2 \text{Var}\big[N(\mathbf{x})\big] = q^2 L(\mathbf{x}) = q\mu(\mathbf{x}). \tag{2}$$

In summary, if one assumes that the detector does not introduce any other fluctuations besides the Poisson randomness, the local mean and standard deviation are related by

$$\sigma(\mathbf{x}) = q^{1/2} \mu(\mathbf{x})^{1/2}. \tag{3}$$

2.1.2. Blurring from the PSF

The EIT telescope has a pixel size of 2.6 arcsec (1.8 Mm at the center of the Sun). The total PSF of the instrument is the combination of the optical PSF and the pixel shape. The optical PSF of EIT has a full-width-at-half-maximum (FWHM) of less than one pixel (Defise, 1999), and by convolution with the square pixel shape, one can deduce the angular resolution of the instrument on the solar disk. This convolution is close to the nominal 2.6 arcsec angular size of the pixel; see Delaboudinière *et al.* (1995). The signal recorded by one pixel thus corresponds to an average of the photon counts on a well-defined area. Two distinct structures separated by a distance smaller than the instrument PSF width will be mixed. With EIT, the smallest detectable wavelength for a periodic spatial feature is 3.6 Mm. This is the origin of the discussed "spatial noise." DeForest (2007) made a precise study of the averaging effect on loop structures observed with EIT and TRACE. The goal of this section is to use a high-cadence data set to try and recover some information about the spatial modulation of the signal that has been averaged by the PSF.

2.1.3. Flat Field

The CCD detector exhibits inhomogeneities in the response. A map of these inhomo-geneities, called the *flat field* (FF), has been estimated, and the eit_prep procedure of the Solar Software library ssw: http://www.msal.com/solarsoft/ corrects for this nonuniformity. If, however, this correction is biased, the "true" signal S^* will be recorded as $S = S^* + \epsilon S^*$, where ϵ is the relative bias in the FF correction estimate. This bias $\epsilon = \epsilon(\mathbf{x})$ fluctuates in space, so it can be considered as a random noise. Because of this bias, the recorded signal $[S(\mathbf{x})]$ corresponding to an ideal flat, uniform source $[S^*(\mathbf{x}) = S_0]$ will exhibit a linear rela-tionship between its spatial mean and standard deviation. This can be shown as follows. Let us consider a small neighborhood $[\mathcal{N}(\mathbf{x})]$ of some point $(\mathbf{x})$. The spatial variance of S over $\mathcal{N}(\mathbf{x})$ is

$$\mathrm{Var}_{\mathcal{N}(\mathbf{x})}(S) = S_0^2 \, \mathrm{Var}_{\mathcal{N}(\mathbf{x})}(\epsilon). \tag{4}$$

Hence the relationship between *spatial* mean (μ) and standard deviation (σ) of the signal (S) over $\mathcal{N}(\mathbf{x})$ is equal to

$$\sigma = k_{\mathrm{FF}}(\mathbf{x}) \cdot \mu, \tag{5}$$

where $k_{\mathrm{FF}}(\mathbf{x}) = \sqrt{\mathrm{Var}_{\mathcal{N}(\mathbf{x})}(\epsilon)}$ is called here the *flat-field noise factor*, which varies from one pixel to another. This reasoning generalizes to nonuniform $S^* \neq S_0$ as long as the intensity in the neighborhood stays fairly uniform. For highly varying photon counts, the influence of ϵ becomes negligible with respect to solar variability.

2.1.4. Read-out Noise

The electronics that converts photon counts to digital number generate a read-out noise of Gaussian nature. Its standard deviation can be estimated but its influence becomes important only for small values of the radiance. Finally, the *thermal noise* (variability of the dark current) originates from the fluctuations of charges generated electronically. However, at EIT operational temperature, it is negligible.

2.2. Method

We consider the Joint Observing Program (JOP-020) recorded by EIT on 4 October 1996 in the 19.5-nm bandpasses. This JOP was dedicated to the observation of nanoflares. It consists of 89 images of size 128×192 pixels with one-minute cadence. One pixel corresponds to a surface of $(1800 \, \mathrm{km})^2$ on the Sun. We consider level-1 images, preprocessed and calibrated through the eit_prep procedure of the ssw library.

 We make use of this high-cadence data set to estimate subpixel variability (sometimes called an "aliasing effect"). To this end, we use *time*-average estimates of the mean and standard deviation computed at each pixel. Indeed, proceeding on a pixel-by-pixel basis ensures that the subsequent results are not contaminated by the flat-field noise. Moreover, the one-minute cadence gives access to subpixel information that is masked by the averaging effect of the PSF in individual images: The solar rotation induces a displacement of one pixel in the horizontal direction every 15 minutes in EIT images; there is thus a displacement of about 1/15 of a pixel per minute. Hence the mean and STD computed on *temporal windows* of 15 minutes give us insight into the subpixel *spatial* statistics, as well as into the temporal variability.

   The JOP sequence shows bright points together with more uniform areas (see Figure 1). These two types of structures are likely to behave differently at subpixel scales: Bright points will typically evolve more quickly than uniform regions showing few signs of activity. Hence we consider separately these two types of regions, as explained in Section 2.3. Section 2.4 proposes a regularity analysis of the data set and shows how it allows us to give scenarios for the evolution of the local SNR and mean–STD relationship across scales.

2.3. Regularity Analysis Using Pointwise Hölder Exponents

To distinguish between regions of high and low regularity in a signal (g), it is customary to compute the pointwise Hölder exponent (h) at each point ($\mathbf{x}_0$). This exponent precisely characterizes the local regularity: a function g is Hölder regular with exponent $h(\mathbf{x}_0)$ at some point $\mathbf{x}_0$ if $|g(\mathbf{x}) - g(\mathbf{x}_0)| \sim |\mathbf{x} - \mathbf{x}_0|^{h(\mathbf{x}_0)}$ for $\mathbf{x}$ in the neighborhood of $\mathbf{x}_0$.[1] If the function is locally C^∞ in a neighborhood of $\mathbf{x}_0$, then $h(\mathbf{x}_0) = +\infty$. If the function is locally similar to a δ-function, then $h(\mathbf{x}_0) = 0$. If $h(\mathbf{x}_0) \geq 1$, the function is at least first-order differentiable. In broad terms, the smaller $h(\mathbf{x}_0)$ is, the more singular the image around $\mathbf{x}_0$ will be. The Appendix provides a precise definition of $h(\mathbf{x}_0)$.

   In Delouille *et al.* (2005), we used a local scale measure computed with the Mexican Hat wavelet transform to estimate the local Hölder exponent. In the present paper, we choose to compute each $h(\mathbf{x}_0)$ through a series of bivariate regressions on spatial windows of increasing sizes. The signal g considered is not the gray-level pixel value of the image, but rather the cardinal of the largest subset of pixels having the same gray level. With this implementation, values for the Hölder exponents range between zero (where the signal behaves like a δ-function) and two (where the signal is twice differentiable). The FracLab software (http://www2.irccyn.ec-nantes.fr/FracLab/; Véhel and Legrand, 2004) was used to compute the values of h.

   Figure 1 shows the image recorded by EIT on 4 October 1996 at 07:39:10 in the 19.5-nm bandpass, together with its map of pointwise Hölder exponents. In our analysis to follow, we discard pixels with Hölder exponent less than 0.2. Therefore cosmic-ray hits, which typically behave like discontinuous δ-functions, are not taken into account.
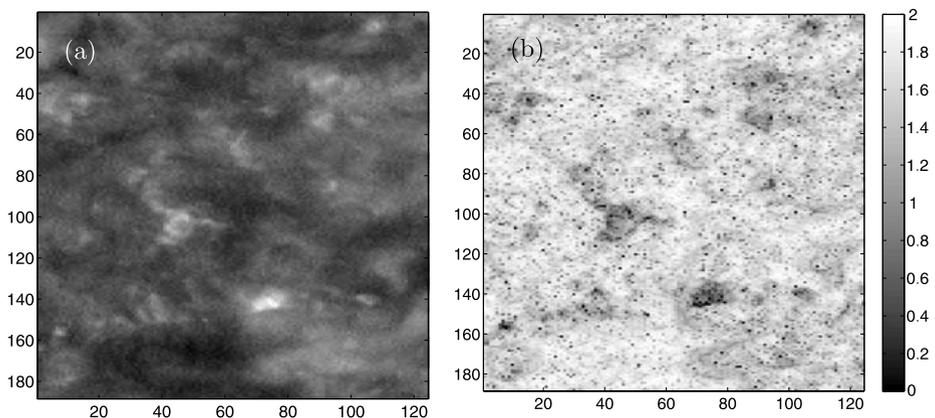

Figure 1   (a) Image from JOP nanoflares data set taken on 4 October 1996 at 07:39:10 (in logarithmic scale). (b) Map of local Hölder exponents computed from the corresponding linear image.

---

[1] Here "$\sim$" denotes an asymptotic proportionality as $\mathbf{x} \to \mathbf{x}_0$.

2.4. Signal-to-Noise Ratio and Relationship between Mean and Standard Deviation

We distinguish two sets of pixels with different regularities: one set of pixels where the image is somewhat smooth and the other where it is more singular. The first set contains all pixels for which the Hölder exponent is greater than 1.6 (smooth regions), and the second set contain all pixels for which the Hölder exponent is smaller than 0.6 (singular regions) but larger than 0.2 (to avoid cosmic rays).

We are interested in the fluctuations of the intensity measured by a pixel of size a located at $\mathbf{x}_0$. For an homogenous Poisson process of intensity L observed at scale a, it is a classical result (Snyder and Miller, 1991) that the mean intensity measured in one pixel is $\mu_a = La^2$ and the variance is $\sigma_a^2 = La^2$ and so $\sigma_a = \mu_a^{1/2}$. In this case, one usually defines a signal-to-noise-ratio by SNR $= \mu_a/\sigma_a = \sqrt{L}\, a \sim a$. By analogy, we focus on the relationship between the temporal mean $[\mu_a(\mathbf{x}_0)]$ and the standard deviation $[\sigma_a(\mathbf{x}_0)]$ of the function f at some given position $(\mathbf{x}_0)$ observed at resolution a. The purpose of the present analysis is to get insight into the evolution of the SNR$_a(\mathbf{x}_0) = \mu_a(\mathbf{x}_0)/\sigma_a(\mathbf{x}_0)$ as the resolution a changes. As already stated, we estimate μ_a and σ_a for each pixel separately by averaging the observed pixel values over nonoverlapping temporal windows of 15 minutes. Since the rotation induces a displacement of one pixel in 15 minutes, our statistics actually cover an area equivalent to two pixels. Hence this technique allows us to see what happens at scales below two EIT pixels, that is, at subresolution scale.

To extract the predominant relationship between the observed μ_a and σ_a, we compute the two-dimensional (2D) histogram of $(\log\mu_a, \log\sigma_a)$. In Figure 2, this histogram is represented in gray levels: Brighter values at coordinate $(\log\mu_0, \log\sigma_0)$ indicate more pixels in the original data set for which $\mu_a = \mu_0$ and $\sigma_a = \sigma_0$. In other words, Figure 2 provides an estimate of the 2D probability density function of the vector $(\log\mu_a, \log\sigma_a)$. In Figure 2a the 2D density estimation of $(\log\mu, \log\sigma)$ corresponds to pixels in singular regions $[h(\mathbf{x}_0) \leq 0.6]$, whereas Figure 2b shows the 2D density for pixels belonging to smooth regions $[h(\mathbf{x}_0) \geq 1.6]$. We computed these 2D densities as a succession of 1D density function estimations of the standard deviation (represented in the y-axis). Each 1D density estimation is carried out on a slice of width $\Delta\mu$ equal to $\log(\Delta\mu) = 0.016$ (in DN s^{-1}). For each slice, we compute the mode (*i.e.,* the maximum) of the 1D density function of the standard deviation. Next, we estimate the line ($\log\sigma_a = k + b_1 \log\mu_a$) that fits these modes. The slope
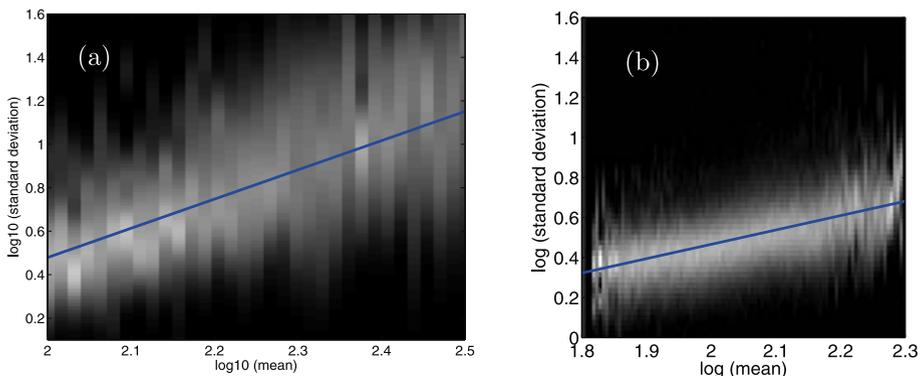

Figure 2 Density estimation for $(\log\mu, \log\sigma)$ for (a) pixels having a Hölder exponent less than 0.6 (representing singular regions) and (b) pixels having a Hölder exponent larger than 1.6 (representing smooth regions). The value of the slope is equal to 1.3 in (a) and to 0.7 in (b).

(b_1) obtained by the least-squares method is equal to 1.3 in the case of singular regions versus 0.7 for smooth regions. Note that it is not possible to disentangle spatial from temporal variability in the interpretation of these values. Although we keep in mind that both types of variability might be present, for the sake of clarity we omit in the notation in the following the temporal dependence of the intensity f.

The standard deviation, or intensity fluctuations, at scale a and location $\mathbf{x}_0$ can be approximated as

$$\sigma_a(\mathbf{x}_0) \sim \left| f(\mathbf{x}_0 + a\mathbf{u}) - f(\mathbf{x}_0) \right|, \tag{6}$$

where $\mathbf{u}$ is any unitary vector. As a direct consequence of the definition of the Hölder exponent $h(\mathbf{x}_0)$, we then have $\sigma_a(\mathbf{x}_0) \sim a^{h(\mathbf{x}_0)}$. The local Hölder regularity helps us in providing a scenario for the evolution of the local SNR as follows.

In smooth regions, the image is rather regular and neighboring pixels have similar values, close to a constant $f(\mathbf{x}_0)$ times the pixel area. Therefore, the mean value observed at scale a around $\mathbf{x}_0$ is roughly proportional to the surface of the pixel, so $\mu_a(\mathbf{x}_0) \sim a^2$ or equivalently $a \sim \mu_a(\mathbf{x}_0)^{1/2}$. As a consequence, for $h(\mathbf{x}_0)$ close to 1.6 [recall that $1.6 \leq h(\mathbf{x}_0) < 2$] we obtain a $\mu - \sigma$ relation of the type

$$\sigma_a(\mathbf{x}_0) \sim a^{1.6} \sim \mu_a(\mathbf{x}_0)^{1.6/2} \sim \mu_a(\mathbf{x}_0)^{0.8}. \tag{7}$$

The 0.8 exponent is close to the observed $\sigma_a \sim \mu_a^{0.7}$ and is greater than the 1/2 exponent that would be observed for a homogeneous Poisson noise. Notice that the Hölder exponent was computed on the original image by using scales above the pixel size, whereas the slope b_1 is representative of the evolution at subresolution scale. Under the approximation (6), the value of the Hölder exponent can be related to the slope b_1; this suggests that there is some consistency between the evolution at super- and subpixel resolution.

Considering now the SNR, one would expect that

$$\mathrm{SNR}_a(\mathbf{x}_0) = \frac{\mu_a}{\sigma_a} \sim a^{2-1.6} \sim a^{0.4} \tag{8}$$

in such regions. As a consequence, the SNR defined above would go to zero as $a^{0.4}$ (as $a \to 0$). This is yet slower than the usual property of Poisson noise for which $\mathrm{SNR}_a \sim a$.

In singular regions for which $h(\mathbf{x}_0) < 0.6$, the singularity corresponds to either a local minimum or a local maximum. We observe that the value of μ_a is about twice as large ($\log_{10} 2 \approx 0.3$) in singular regions ($h < 0.6$) as in smooth regions ($h > 1.6$) (see the values of $\log \mu_a$ in Figure 2a, which range from 2 to 2.5, compared to Figure 2b, where they range from 1.8 to 2.3 for smooth regions). Thus these singular regions correspond mostly to local maxima.

As a consequence, the intensity in regions where $h(\mathbf{x}_0) < 0.6$ is peaked: The extreme case would be that of a δ-function, where the intensity would be infinitely concentrated at some unique position. Therefore, the mean (μ_a) is dominated by some extreme value associated with a small region of emission. Then one would expect that $\mu_a \sim a^{\varepsilon}(\mathbf{x}_0)$ with $\varepsilon(\mathbf{x}_0) < 2$ (if the image is locally a δ-function, μ_a is constant, and $\varepsilon = 0$); equivalently, one then has $a \sim \mu_a^{1/\varepsilon}$. Hence for $h(\mathbf{x}_0) \simeq 0.6$ we get

$$\sigma_a \sim a^{0.6} \sim \mu_a^{0.6/\varepsilon} \sim \mu_a^{1+\beta}, \tag{9}$$

where $\beta > 0$ as soon as $\varepsilon < 0.6$. This argument is consistent with the observed value of $b_1 = 1.3 = 1 + 0.3$ [which would typically correspond to $h(\mathbf{x}_0) = 0.6$ and $\varepsilon = 0.46$].

For the SNR, one would expect for such singular regions that

$$\text{SNR}_a = \frac{\mu_a}{\sigma_a} \sim a^{\varepsilon - 0.6}. \tag{10}$$

Therefore, in the particular case when $\varepsilon < 0.6$, one would even get that $\text{SNR}_a \to \infty$ as $a \to 0$. Locally, at places where there are δ-function structures, the SNR would increase as the scale becomes smaller. In practice, the limit $a \to 0$ needs to be considered with caution in the present approach. Our argument remains valid only when the scale of observation remains much greater than the typical scale of the singular object we focus on. As soon as the resolution becomes sufficient to resolve an elementary object, it will appear as "smooth" rather than "singular." The singularity or smoothness of a region is a notion relative to the scale of observation. The argument here simply tells us that one may expect some gain, or at least a slow decrease, in SNR as the resolution gets finer around regions that appear singular at the present scale of observation; for example, if $h(\mathbf{x}_0) = 0.6$ and $\varepsilon < 1$, the SNR will decrease following a power law with exponent smaller than 0.4 as $a \to 0$.

This qualitative study suggests that modeling images of the Sun by some homogeneous Poisson process leads to a pessimistic prediction of the evolution of the local SNR when decreasing the scale of observation, that is, when observing at a finer resolution. The use of a uniform intensity for the Poisson process neglects the spatial fluctuations of the emission coming from the Sun. Taking into account the local regularity of the image by using the Hölder exponent allows us to make more precise predictions about this evolution: The resulting prediction is less pessimistic since we get $\text{SNR}_a \sim a^\gamma$ with $\gamma < 1$ in place of the usual $\text{SNR}_a \sim a$ ($\gamma = 1$) predicted by the Poisson-noise model. The more singular the region of interest is, the slower will be the decrease in SNR as the resolution gets finer. This is important information for assessing the quality of forthcoming high-resolution observations, since these might be threatened by the SNR decreasing too fast as the resolution gets higher. In particular, in the context of the SO mission, radiometric models assessing the number of photons available per pixel at HRI resolution should take into account the spatial and temporal fluctuations of the radiance.

3. Forward Modeling Approach

In this section, we model the solar corona as a superposition in space and time of a large number of flarelike events, characterized by their surface, duration, intensity, and localization. Having fixed a probability distribution function for these quantities, we generate a time series of images. We then compute the mean (μ) and standard deviation (σ), either in space (over the whole image) or in time (over the whole sequence). In both cases, we estimate the parameters (b_0, b_1) of the model $\sigma = b_0 \mu^{b_1}$. We repeat this operation for several values of the power-law index characterizing the distributions of flarelike events. We then relate the value of b_1 to these indices. This allows us to identify which flare characteristics (area, duration, and/or intensity) most influence the relationship between mean and standard deviation.

The spatial and temporal resolution of the fine-grid data sequence corresponds to the expected resolution of HRI at perihelion, namely a pixel size of (80 km) and a cadence of one second. This is approximately five times better spatial resolution than what the TRACE instrument provides and a 25 times enhancement as compared to the EIT telescope.

3.1. Generation of the Data Sequence

We begin by describing how to generate a flarelike event. To handle the simulation within a reasonable time scale, we simplify the physics and especially the behavior of the cooling phase: An event is a cube with a constant intensity within a given spatial and temporal window and a zero value outside. In future studies, we plan on using more sophisticated models for the time evolution of an event.

We need to choose a probability distribution for the area, duration, and intensity of an event. Past measurements of bright events point at scale invariance of these three characteristics; their distribution is therefore usually modeled by a power law (see, *e.g.*, Crosby *et al.*, 1993). In our simulation, the area (A), duration (D), and intensity (I) characterizing an event follow such a power-law distribution:

$$p(A) \propto A^{\alpha}, \qquad p(D) \propto D^{\tau}, \qquad p(I) \propto I^{\gamma}, \qquad (11)$$

where $p(x)$ denotes the probability density function of the quantity x.

Different values for (α, τ, γ) are proposed in the literature. Values for the power-law index of the peak flux (γ), or emission measure, differ the most: Aschwanden and Parnell (2002) observe values ranging between -1.75 and -1.94 for the peak flux in TRACE and *Yohkoh*/SXT, whereas Crosby *et al.* (1993) provide a value of -1.59 for the peak HXR flux power slope. However, Parker's hypothesis conveying the idea that the solar corona could be heated by a multitude of nanoflares needs a slope of at most -2 for the thermal energy content. Krucker and Benz (1998) give a value of γ ranging between -2.6 and -2.3; avalanche models produce a slope of -2.4 (Viticchié *et al.*, 2006) and even -3.5 for the smallest flare (Vlahos *et al.*, 1995). Studies exploring the values for the power law of the area, α, include that of Aschwanden and Parnell (2002), who derived values of -2.45 and -1.86. Finally, values for the duration index τ range from -1.95 (Crosby *et al.*, 1993) to -8 (Paczuski *et al.*, 2005) and even -11 (Vlahos *et al.*, 1995) for small flares. To be consistent with these different results, we explore all combinations of values for α, τ, γ given in Table 1.

We now specify the range of values for A, D, and I, as well as their relationships. Berghmans *et al.* (1998) used a one-minute cadence data set recorded by EIT on 28 December 2006 and found that the area and duration of a brightening are almost linearly correlated in a $\log - \log$ plot. However, the typical duration of an 80-km event is unclear. Lin *et al.* (1984) reported X-ray microflares lasting from a few seconds to several tens of seconds and having a power-law energy spectra. Golub *et al.* (1989) computed ionization times of the order of two to four seconds for the Fe IX, Fe X, and Fe XI ions, whereas the cooling time was of the order of several minutes. We decided to choose intervals of values for the area and duration that are compatible with a straightforward extrapolation of the results in Berghmans *et al.* (1998). Areas range between 0.0064 and 100 Mm^2 (covering from 1 to 125^2 pixels in the fine grid), and the duration of an event may last between one second and five minutes. This simplified setting is easily implemented, but in a further study, we plan to consider other types of extrapolations of the distribution of events at smaller scales and to take into account the exponential decay of the cooling phase. Finally, the intensity (in arbitrary units) is allowed to span five orders of magnitude, in agreement with the results of Aschwanden and Parnell (2002) on the relationship between area and intensity. Table 1 summarizes these ranges.

The "high-resolution" data sequences contain 300 temporal frames, each with a spatial extent of 500×500 pixels. They are simulated as the superposition of a large number (N) of events, so that the entire space is filled with events. An event is modeled as a cube in

Table 1 Power-law indices and ranges for the area, duration, and intensity considered in the simulation.

	Power-law index	Range
Area	$\alpha \in \{-1.5, -1.6, -1.9, -2.9\}$	$[0.0064 - 100 \text{ Mm}^2]$ or $[1 - 125^2]$ pixels
Duration	$\tau \in \{-2.1; -2.5; -4, -8\}$	$[1 - 300 \text{ s}]$ or $[1 - 300]$ frames
Intensity	$\gamma \in \{-1.6; -1.8; -1.95; -2.3; -3.5\}$	$[1 - 10^5]$ (arbitrary units)

Table 2 Coarsening factors operated in the simulation.

Data cube	Spatial dimension (in pixels)	Time dimension (number of frames)	ρ: size generated/size rebin
Generated	500×500	300	1
Rebin 1	100×100	5	1500 ($\approx$ TRACE)
Rebin 2	20×20	5	37500 ($\approx$ EIT, 1-min cadence)

the spatio-temporal dimension: It has a constant intensity within this data cube and a zero intensity outside. The data sequences are generated as follows:

1. Choose a particular combination of values for α, τ, and γ.
2. Using the prescribed power-law distributions (index value and range), generate N values for A, D, and I.
3. Rank the N values generated for A, D, and I by increasing order. A flarelike event is characterized by the triple $(A_{(k)}, D_{(k)}, I_{(k)})$, $k = 1, \ldots, N$, where $X_{(i)}$ denotes the ith element of the order statistics of X (*i.e.*, $X_{(1)} \leq X_{(2)} \leq \cdots$). With this ordering, an event with small area will have also a small duration and intensity.
4. Generate the localization in space and time of the N events as independent samples from a uniform distribution.
5. Obtain the data sequence by superpositioning the N events.

Note that, in the third step, we do not impose a deterministic relationship among A, D, and I. Indeed, there is a large dispersion around the linear fit between area and duration of observed brightenings (*cf.* Berghmans *et al.*, 1998). This means that there is a range of possible durations for a given event size.

We consider three values for the number of events generated: $N = 10^5$, 10^7, and 5×10^7. For each of these three values, we generate two data sequences. In total, for a given set of parameters (α, τ, γ), we thus generate six data sets.

From the high-resolution data cube, we derive two coarser resolution data sets that reflect, respectively, TRACE and EIT resolution: A rebin by a factor five in space and 60 in time is close to the specifications of TRACE, whereas a rebin by a factor 25 in space emulates EIT's spatial resolution. These two rebinning factors (ρ) are displayed in Table 2. Recall that the spatial rebin emulates the PSF operator, which is assumed here to be a step function. The temporal rebinning simulates the integration over time during an image acquisition.

A pixel in a rebinned image is termed a "macro-pixel." Because the localization of each event is generated randomly, there will be a different number of events in each macro-pixel. This introduces another source of variability: When averaging to obtain the rebinned image, the sum is performed over a random number of events in each macro-pixel. Figure 3a shows one realization with $N = 10^5$ events and the smallest power-law indices in absolute value ($\alpha = -1.5$, $\tau = -2.1$, $\gamma = -1.6$). This setting generates values for the area, duration,
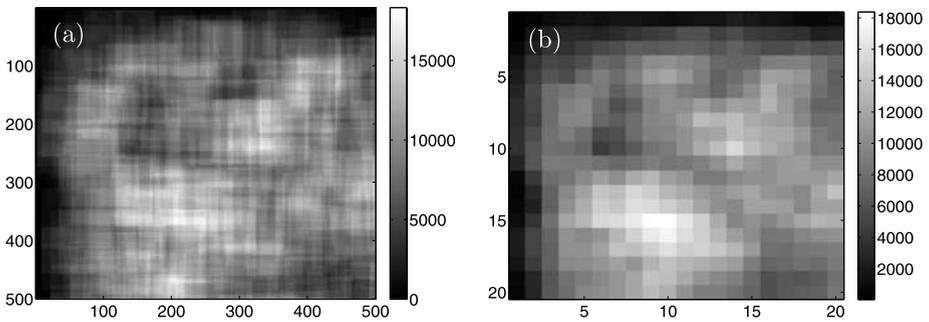
Figure 3 Example of one realization, with $N = 10^5$, $\alpha = -1.5$, $\tau = -2.1$, and $\gamma = -1.6$. (a) A high resolution image; (b) the corresponding image rebinned by a factor of 25×25 in space and 60 in time. The values of the intensity are in arbitrary units.

and intensity that cover a large range. Structured regions appear as a consequence of the superposition of events of diverse sizes. These fine structures are largely smoothed out in the rebinned version displayed in Figure 3b.

3.2. Phenomenological Model

For each coarse-resolution data set, the following quantities are considered: μ_S and σ_S are an average (over time) of the mean and STD computed over *space* on each frame of the sequence; μ_T and σ_T are an average (over space) of the *temporal* mean and STD computed for each pixel. We summarize the six values of the same combination of $(\alpha, \tau, \gamma, \rho)$ by estimating the slope and intercept of a linear regression between $\log(\sigma)$ and $\log(\mu)$:

$$\log \sigma_S = b_{0,S} + b_{1,S} \log \mu_S, \tag{12}$$

$$\log \sigma_T = b_{0,T} + b_{1,T} \log \mu_T. \tag{13}$$

All the linear regressions done to estimate $(b_{0,S}, b_{1,S})$ and $(b_{0,T}, b_{1,T})$ have a R^2 goodness of fit larger than 0.96.[2] We may thus consider that the model $\sigma = b_0 \mu^{b_1}$ is valid.

We model the slopes $b_{1,S}$ and $b_{1,T}$ as a function of α, τ, γ, and ρ to see which parameters have the most influence on these slopes. We do not analyze the behavior of the intercept b_0 since this quantity is not based on any physical model and cannot be physically related to observations. We consider a simple linear model for $b_{1,T}$ and $b_{1,S}$:

$$b_1 = c_0 + c_1 \alpha + c_2 \tau + c_3 \gamma + c_4 \rho + \epsilon. \tag{14}$$

Variables are standardized before entering the model: They are centered and divided by their half-range. This facilitates the interpretation of coefficient values **c**: The constant parameter c_0 gives the response value at the center of the hypercube (*i.e.,* for a mean value of α, τ, γ, and ρ). The coefficient before a variable X in the model indicates an average increase of the response when X increases from the center of the domain to its maximum.

---

[2]The R^2 statistic, $R^2 \in [0, 1]$, is the ratio between the variance explained by the model and the total variation the observations. $R^2 = 1$ means that the model fits the data perfectly (Chatterjee and Hadi, 1986).

Table 3 Coefficient values and standard deviations for the linear models explaining the responses $b_{1,S}$ and $b_{1,T}$, respectively. NS stands for "nonsignificant": A star in this column indicates a parameter that can be omitted in the model at the 0.05 level. The slope $b_{1,S}$ is mostly driven by the power-law index for the area, whereas the duration influences $b_{1,T}$ the most.

Variable	$b_{1,S}$	STD($b_{1,S}$)	NS	$b_{1,T}$	STD($b_{1,T}$)	NS
CONST	0.756	0.0055		0.709	0.0100	
α	0.156	0.0070		0.056	0.0126	
τ	0.022	0.0070		0.172	0.0126	
γ	-0.001	0.0078	*	-0.016	0.0140	*
ρ	0.008	0.0055	*	0.012	0.0100	*
R^2 statistics	0.57			0.91		

3.3. Results of the Simulation Study

Table 3 shows the estimation of the regression coefficients c_i in Equation (14) together with an estimate of their uncertainty. We entered in the model the values $\rho = \{15, 375\}$ for the rebin factor.

A linear model for the slope $b_{1,S}$ seems satisfactory since $R^2 = 0.77$. The constant parameter represents the value of $b_{1,S}$ for a mean value of α, τ, γ, and ρ among the range of values considered. This constant is equal to 0.75 and is thus above the 0.5 value that we would obtain in case of a homogeneous Poisson process. The variable that influences $b_{1,S}$ the most is the power-law index for the area; the duration has a smaller influence, whereas both the power-law index for the intensity (γ) and the rebin parameter (ρ) are statistically nonsignificant. With a value of $\alpha = -3$ (and all other parameters kept at their mid-values), mainly small events are generated. The slope $b_{1,S}$ then decreases down to 0.6, close to the situation of a homogeneous Poisson process. When α grows to $\alpha = -1.5$, larger events are generated as well, and the superposition of large and small events produces a more inhomogeneous process: The value of $b_{1,S}$ then increases up to 0.9.

If one now considers the slope $b_{1,T}$, the results of Table 3 indicate that the duration τ mainly influences the evolution of the mean and STD computed over *time*. In this case, the goodness of fit is relatively low ($R^2 = 0.57$). Figure 4 shows how $b_{1,T}$ and $b_{1,S}$ evolve as a function of α and τ, with γ kept fixed ($\gamma = -1.6$), and for a rebinned data set of size $100 \times 100 \times 5$. A quadratic model seems more appropriate for the slope $b_{1,T}$. If we fit a quadratic model of the type

$$b_{1,T} = c_0 + c_1\alpha + c_2\tau + c_3\gamma + c_4\rho + c_{11}\alpha^2 + c_{22}\tau^2 + c_{33}\gamma^2 + \epsilon \qquad (15)$$

we obtain an acceptable $R^2 = 0.81$. Within the quadratic terms, only the coefficient for τ^2 is significant. The parameter τ influences $b_{1,T}$ similarly to how α influences $b_{1,S}$: When τ is equal to -2.1, the slope $b_{1,T}$ increases to 0.87; when $\tau = -8$ the slope decreases to 0.63 (with all other parameters kept fixed at their mid-values). The parameter α also influences $b_{1,T}$, but to a lesser extent. The intensity and rebin factor are again statistically nonsignificant.

In summary, we observe that *i*) the relationship between spatial mean and standard deviation is mostly affected by the distribution of areas of the events, *ii*) temporal mean and standard deviation are driven mostly by the temporal dynamics, *iii*) the intensity distribution does not seem to play a significant role, *iv*) we observe no strong effect of the coarsening factor.
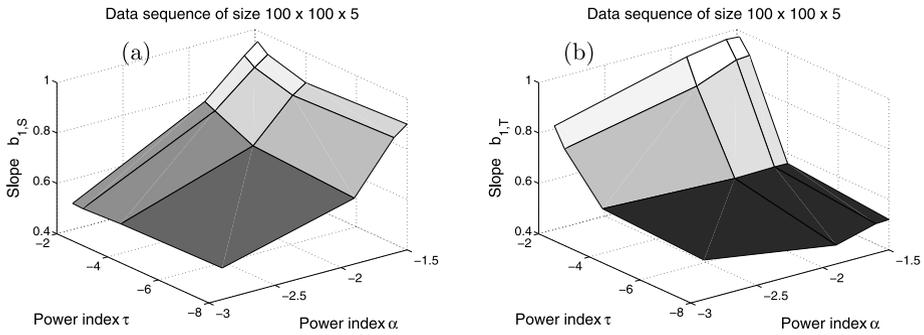
Figure 4 Variation of the slopes $b_{1,S}$ (a) and $b_{1,T}$ (b) as a function of α and τ. The value for γ is fixed and equal to -1.6. Here the rebin factor was equal to $\gamma = 1500$ (*i.e.*, the coarsened data set is of size $100 \times 100 \times 5$).

4. Discussion and Conclusion

We proposed a way to extract subpixel information in a one-minute-cadence EIT data set, and we derived a scenario for the variation of the SNR as the scale of observation becomes smaller. Taking into account the variability in the emission process, we showed that the local SNR decays much more slowly in singular regions (where the variability is larger) than in smooth regions (characterized by a more uniform emission). We observed in both cases that the slope between standard deviation and mean is above 0.5 and that the SNR degrades more slowly than in the case of a uniform Poisson process.

Next, we investigated how the mean–variance relationship evolves with different theoretical distribution of nanoflare parameters. A small index for the power-law distribution of the area favors small events and generates a process close to a homogeneous Poisson distribution. When a large disparity of areas is allowed in the simulation of events (by choosing a large value for the power-law index), more inhomogeneous structures appear. These are averaged at coarser resolution and create "spatial noise." The slope $b_{1,S}$ in a graph representing the spatial standard deviation against the mean has in this case a value close to one. In a parallel way, when the distribution (D) generates a large range of durations, the temporal mean–STD relationship exhibits a slope larger than what is observed for a homogeneous Poisson process.

The determination of solar variability (such as, *e.g.*, microflaring or the determination of coronal loop width) at the limit of instrument measure often requires a careful analysis to separate noise components from true solar variability. We now relate our work to several other methods presented in the literature.

Aschwanden *et al.* ([2000](#)) evaluate the level of different sources of instrumental noise in the TRACE instrument: read-out, digitization, compression, and dark-current subtraction noise. In addition to these noises, whose levels are independent of the flux, they estimate two other noise components that depend on the flux level: the Poisson noise and the error coming from the removal of cosmic-ray hits. However, they did not apply a flat-field correction to pixels, and hence their estimates are not subject to the flat-field noise described in Section [2.1](#).

Our data analysis did not assume a particular photon-noise distribution; it was meant to be as generic as possible. Katsukawa and Tsuneta ([2001](#)) took another approach in their study of the time profile of X-ray intensities using *Yohkoh*/SXT. They first derive for each

pixel its time profile and mean background intensity (I_0), and they used this value to estimate the standard deviation of the photon noise (σ_P). Next, they estimate the standard deviation (σ_I) of the time-series profile, assuming the core component has a Gaussian distribution. The ratio σ_I/σ_P increases with the mean profile I_0, and they estimate the relation between the two quantities. They observed that the fluctuations in darker regions ($I_0 \leq 100$ DN) are almost entirely due to photon noise, whereas there are significant fluctuations of solar origin in bright regions ($I_0 \geq 100$ DN). Although the methodology is different, the results in Katsukawa and Tsuneta (2001) parallel our study: Darker regions look typically more uniform, and we observe there a behavior closer to a homogeneous Poisson process than in bright (more irregular) areas.

Finally, DeForest (2007) investigates the effect of random noise and telescope PSF on compact linear structures featuring coronal loops. A forward model of the TRACE PSF indicates that structures with apparent size less than two pixels wide cannot be distinguished visually from structures of zero width. He also studied some particular loops observed by TRACE. Assuming a loop is composed of a set of faint threads, he found an estimate for the size of elementary structures in the lower corona. Similarly, Figure 3 shows how fine structures disappear when observed at lower resolution.

In a forthcoming paper, we will analyze images of the quiet corona using multifractal tools. It is also possible to use multifractal processes to *synthesize* images similar to the quiet-Sun corona at higher resolution than what current telescopes offer. This allows us to make more precise predictions about the SNR that would be available at a given high resolution.

Appendix: Pointwise Hölder Exponent

The Hölder exponent at $\mathbf{x}_0$, denoted $h(\mathbf{x}_0)$, provides a way to quantify the strength of a singularity of a function g at the point $\mathbf{x}_0$. It is defined in a rigorous way as the largest exponent such that there exists a polynomial of degree $n \leq h(\mathbf{x}_0)$ and a constant $C > 0$ with the property that for any x in a neighborhood of $\mathbf{x}_0$ the following inequality is verified:

$$\left| g(\mathbf{x}) - P(\mathbf{x} - \mathbf{x}_0) \right| \leq C |\mathbf{x} - \mathbf{x}_0|^{h(\mathbf{x}_0)}. \tag{A1}$$

When g is n-times differentiable at $\mathbf{x}_0$, the polynomial $P(\mathbf{x} - \mathbf{x}_0)$ is simply the Taylor expansion polynomial of $g(x)$ at x_0; in this case, $h(\mathbf{x}_0) > n$. If $h(x_0) < 1$ the polynomial $P(x - x_0)$ simplifies to $g(x_0)$. A well-known example is given by the function $g(x) = a + b|x - x_0|^\gamma$, whose Hölder exponent at x_0 is given by γ (when γ is not an even integer). In general, the higher h is, the more regular is the function g. Conversely, the smaller h is, the more singular is the function g.

References

Aschwanden, M.J., Parnell, C.E.: 2002, Nanoflare statistics from first principles: Fractal geometry and temperature synthesis. *Astrophys. J.* **572**, 1048 – 1071.

Aschwanden, M.J., Nightingale, R.W., Tarbell, T.D., Wolfson, C.J.: 2000, Time variability of the "quiet" sun observed with TRACE. I. Instrumental effects, event detection, and discrimination of extreme-ultraviolet microflares. *Astrophys. J.* **535**, 1027 – 1046.

Berghmans, D., Clette, F., Moses, D.: 1998, Quiet Sun EUV transient brightenings and turbulence. A panoramic view by EIT on board SOHO. *Astron. Astrophys.* **336**, 1039 – 1055.

Chatterjee, S., Hadi, A.S.: 1986, Influential observations, high leverage points, and outliers in linear regression. *Stat. Sci.* **1**, 379 – 416.

Crosby, N.B., Aschwanden, M.J., Dennis, B.R.: 1993, Frequency distributions and correlations of solar X-ray flare parameters. *Solar Phys.* **143**, 275 – 299.

Defise, J.M.: 1999, Analyse des performances instrumentales du téléscope spatial EIT. Ph.D. thesis, Université de Liège.

DeForest, C.E.: 2007, On the size of structures in the Solar corona. *Astrophys. J.* **661**, 532 – 542.

Delaboudinière, J.P., Artzner, G.E., Brunaud, J., Gabriel, A.H., Hochedez, J.F., Millier, F., Song, X.Y., Au, B., Dere, K.P., Howard, R.A., Kreplin, R., Michels, D.J., Moses, J.D., Defise, J.M., Jamar, C., Rochus, P., Chauvineau, J.P., Marioge, J.P., Catura, R.C., Lemen, J.R., Shing, L., Stern, R.A., Gurman, J.B., Neupert, W.M., Maucherat, A., Clette, F., Cugnon, P., van Dessel, E.L.: 1995, EIT: Extreme-ultraviolet imaging telescope for the SOHO mission. *Solar Phys.* **162**, 291 – 312.

Delouille, V., Patoul, J., Hochedez, J.F., Jacques, L., Antoine, J.P.: 2005, Wavelet spectrum analysis of EIT/SOHO images. *Solar Phys.* **228**, 301 – 321.

Golub, L., Hartquist, T.W., Quillen, A.C.: 1989, Comments on the observability of coronal variations. *Solar Phys.* **122**, 245 – 261.

Hochedez, J.F., Lemaire, P., Pace, E., Schühle, U., Verwichte, E.: 2001, Wide bandgap EUV and VUV imagers for the Solar Orbiter. In: Battrick, B., Sawaya-Lacoste, H., Marsch, E., Martinez Pillet, V., Fleck, B., Marsden, R. (eds.) *Solar Encounter. Proceedings of the First Solar Orbiter Workshop* **493**. ESA, Noordwijk, 245 – 250.

Isliker, H., Anastasiadis, A., Vlahos, L.: 2001, MHD consistent cellular automata (CA) models. II. Applications to Solar flares. *Astron. Astrophys.* **377**, 1068 – 1080.

Janesick, J., Klaasen, K., Elliott, T.: 1985, CCD charge collection efficiency and the photon transfer technique. In: Dereniak, E.L., Prettyjohns, K.N. (eds.) *Solid State Imaging Arrays (SPIE)* **570**, 7 – 19.

Katsukawa, Y., Tsuneta, S.: 2001, Small fluctuation of coronal X-ray intensity and a signature of nanoflares. *Astrophys. J.* **557**, 343 – 350.

Krucker, S., Benz, A.O.: 1998, energy distribution of heating processes in the quiet Solar corona. *Astrophys. J. Lett.* **501**, 213 – 216.

Lin, R.P., Schwartz, R.A., Kane, S.R., Pelling, R.M., Hurley, K.C.: 1984, Solar hard X-ray microflares. *Astrophys. J.* **283**, 421 – 425.

Paczuski, M., Boettcher, S., Baiesi, M.: 2005, Interoccurrence times in the Bak – Tang – Wiesenfeld sandpile model: A comparison with the observed statistics of Solar flares. *Phys. Rev. Lett.* **95**(18), 181102 – 181105.

Snyder, D.L., Miller, M.I.: 1991, *Random Point Processes in Time and Space*, Springer, New York.

Véhel, J.L., Legrand, P.: 2004, Signal and image processing with fraclab. In: Novak, M. (ed.) *Thinking in Patterns*, World Scientific, Singapore, 321 – 323.

Viticchié, B., Del Moro, D., Berrilli, F.: 2006, Statistical properties of synthetic nanoflares. *Astrophys. J.* **652**, 1734 – 1739.

Vlahos, L., Georgoulis, M., Kluiving, R., Paschos, P.: 1995, The statistical flare. *Astron. Astrophys.* **299**, 897 – 911.